ACS APPLIED MATERIALS & INTERFACES

Research Article

www.acsami.org

Microstructure and Electronic Band Structure of Pulsed Laser Deposited Iron Fluoride Thin Film for Battery Electrodes

Reinaldo Santos-Ortiz,[†] Vyacheslav Volkov,[‡] Stefan Schmid,[†] Fang-Ling Kuo,[†] Kim Kisslinger,[‡] Soumya Nag,[†] Rajarshi Banerjee,[†] Yimei Zhu,[‡] and Nigel D. Shepherd*,[†]

[†]Department of Materials Science and Engineering and Center for Advanced Research and Technology, University of North Texas, Denton, Texas 76203, United States

[‡]Brookhaven National Laboratory, Upton, New York 11973, United States

ABSTRACT: Battery electrodes in thin-film form are free of the binders used with traditional powder electrodes and present an ideal platform to obtain basic insight to the evolution of the electrode−electrolyte interface passivation layer, the formation of secondary phases, and the structural underpinnings of reversibility. This is particularly relevant to the not yet fully understood conversion electrode materials, which possess enormous potential for providing transformative capacity improvements in next-generation lithium-ion batteries. However, this necessitates an understanding of the electronic charge transport properties and band structure of the thin films. This work presents an investigation of the electron transport properties of iron fluoride (FeF_2) thin-film electrodes for Li-ion batteries. FeF_2 thin films were prepared by pulsed-laser deposition, and their phase purity was characterized by electron microscopy and diffraction. The grown materials are polycrystalline FeF_2 with a $P4_2/mnm$ crystallographic symmetry. Room-temperature Hall measurements reveal that as-deposited FeF_2 is n-type: the Hall coefficients were negative, electron mobility was 0.33 $cm^2/(V\ s)$ and resistivity was 0.255 Ω cm. The electronic band diagram of FeF_2 was obtained using a combination of ultraviolet photoelectron spectroscopy, photoluminescence, photoluminescence excitation and optical absorption, which revealed that FeF_2 is a direct bandgap, n-type semiconductor whose band structure is characterized by a 3.4 eV bandgap, a workfunction of ∼4.51 eV, and an effective Fermi level that resides approximately 0.22 eV below the conduction band edge. We propose that the shallow donor levels at 0.22 eV are responsible for the measured n-type conductivity. The band diagram was used to understand electron transport in FeF_2 thin film and FeF_2−C composite electrodes.

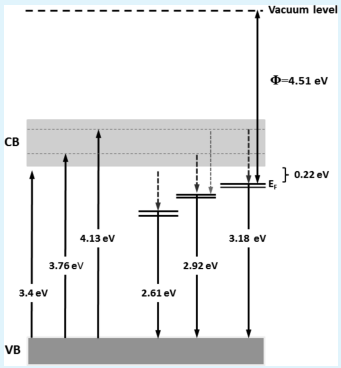

KEYWORDS: *iron fluoride, band diagram, photoluminescence, electron transport, thin-film electrodes, lithium-ion batteries*

INTRODUCTION

Current state-of-the-art Li-ion batteries use intercalation electrodes (e.g., layered $LiCoO_2$, spinel $LiMn_2O_4$, and graphite), wherein the redox reaction is restricted to single-electron transfer. This presents an intrinsic limit to the volumetric and gravimetric energy density that can be achieved. In contrast to traditional intercalation materials, conversion compound electrodes such as FeF_2 permit a reversible change of more than one Li ion per 3d metal cation, which can result in significantly higher capacities than traditional intercalation materials, and are therefore expected to yield transformative improvements in lithium ion battery performance. A comprehensive listing of the theoretical energy capacity for various conversion compounds has been reported.[1,2] Conversion reactions are phase transitions where one parent compound decomposes into two or more products after reaction with lithium. They follow the general equation: $MX_m + n\mathrm{Li} \leftrightarrow \mathrm{M} + n\mathrm{LiX}_{m/n}$, where M = transition metal, X = anion, and n = formal oxidation state of X. Reversible conversion reactions with lithium were first reported in 2000 by Tarascon et al. for transition metal oxides,[3] and later for metal fluorides, sulfides, nitrides, phosphides, and hydrides.[4−8] The highest specific capacity of the electrode is obtained when all of the possible oxidation states of the compound are utilized during the redox cycle, and an increase in the ionicity of the metal−X bond generally increases the output voltage of the conversion reaction.[1] Therefore, the output voltage is expected to be highest for the highly ionic metal fluorides. Because an appropriate anode material should exhibit low voltage vs Li +/Li and a cathode material should exhibit a high voltage, several metal fluorides including FeF_2 are potentially useful as cathodes. The general technical and scientific challenges associated with Li-ion batteries have been reviewed.[9,10]

$LiCoO_2$ intercalation cathode which is used in current state-of-the-art lithium ion batteries has theoretical and practical capacities of 280 mA h g^{-1} and 140 mA h g^{-1}, respectively, in contrast to 773 mA h g^{-1} for FeF_3 bound in graphite,[11] and 571 mA h g^{-1} for FeF_2 in its thin film form.[12] Although the conversion mechanisms in binary metal fluoride powders have been reported recently,[13] basic questions related to the conversion reactions and reversibility remain. A particular hindrance is the presence of binders that are used to facilitate

Received: August 22, 2012
Accepted: February 12, 2013
Published: February 12, 2013

   dx.doi.org/10.1021/am3017569 | ACS Appl. Mater. Interfaces 2013, 5, 2387−2391

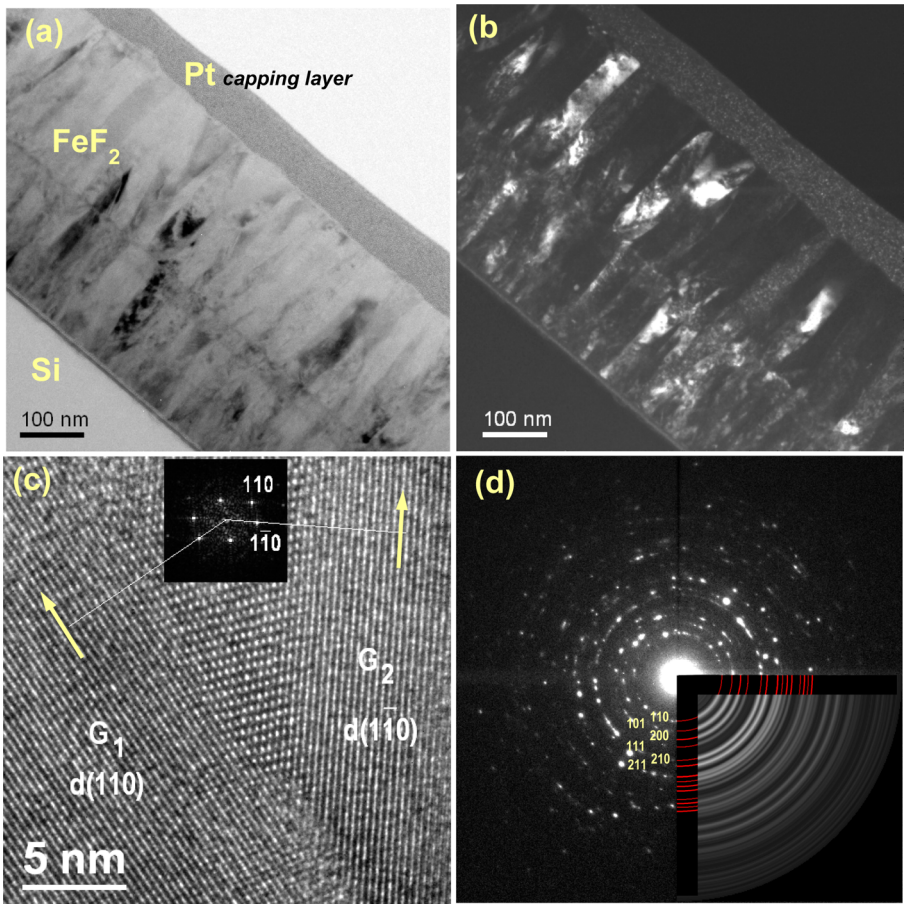

Figure 1. (a) Bright-field TEM image of FeF_2 film grown at 8 J/cm^2 and 10 Hz on a Si substrate at 400 °C; (b) the corresponding dark-field image showing the columnar grain structure. The Pt capping layer protects the specimen during focused ion beam sample preparation; (c) high-resolution TEM image showing the grain overlap; (d) experimental (with rotation averaging shown in inset) and calculated (red lines) SAED patterns indicating the phase purity of the polycrystalline FeF_2. To limit clutter, we indexed only the first six set of planes. Starting from the center these are (110), (101), (200), (111), (210), (211).

electronic conduction in these electrode systems which are traditionally interrogated and employed in their powder form. Binders shroud the understanding of the electrode−electrolyte interface/interphase (SEI) passivation layer growth, of Li agglomeration, and of the formation of new phases under electrochemical cycling. In contrast, thin-film materials are free of the binders used with powders, and present an ideal platform to obtain basic insight to the evolution of the electrode−electrolyte interface passivation layer, and the electrochemical behavior of true complex phases in a controllable manner. From an application standpoint, all solid-state thin-film batteries[14] offer exciting opportunities for direct integration with electronics. However, this implies that from both the basic and application perspectives, the electronic band structure and charge transport properties of conversion compound thin films must be understood to complement the insights obtained from electrochemical studies. Specifically with regard to electrical properties, the thin film electrode material itself must conduct electronic charge, must have suitable band alignment with the current collector to facilitate efficient charge outcoupling and electrochemical cycling, and should not have high concentrations of deep traps that detrimentally limit the electronic charge that can be outcoupled. The optical constants of FeF_2 films have been reported,[15] and its valence band states and binding energies have been examined by photoelectron spectroscopy.[16−18] However, this knowledge is not sufficient to describe a schematic band diagram. Rangan et al.[18] have reported a transport gap of 1.9 eV, and that the bottom of the conduction band is coincident with the Fermi level (Figure 1, ref 18). Such an alignment between the Fermi level and conduction band edge is only expected in materials with metallic or degenerate n-type electrical conduction, and should probably be reexamined. Although as a general principle the high ionicity of the Fe−F bond is expected to produce a large bandgap, a review of the literature indicates that the specifics of the FeF_2 schematic band diagram (and the other conversion compound metal fluorides) have not been reported, which served as the motivation for this study.

EXPERIMENTAL SECTION

FeF_2 ablation targets were fabricated by pressing anhydrous FeF_2 powder and sintering the green compact at 650 °C for 60 min under a flow of ultrahigh purity nitrogen. Films were then deposited onto oxide-etched Si (100) and glass substrates using the 248 nm line of an Excimer laser operating at 10 Hz with a fluence of 8 J/cm^2 for structural, optical, and electrical characterization. The substrate temperature was 400 °C and the base pressure of the system was 1 × 10^{-8} Torr. These conditions produced films that were nearly stoichiometric at a growth rate of ∼6 nm/min. We shall present the details of the process optimization study elsewhere. The structure and phase purity of the deposited FeF_2 films was characterized using a JEOL 3000F field-emission transmission electron microscope (TEM). Workfunction was determined by ultraviolet photoelectron spectros-

copy (UPS) with a PHI 5000 Versaprobe UPS/XPS spectrometer using He−Iα 21.22 eV and He−II 40.8 eV UV light was used to probe the valence band structure. Prior to UPS measurements the sample surfaces were cleaned in situ by Ar sputtering (2 kV, 2 μA beam, 3 mm × 3 mm area, sputter rate ∼4 nm/min) for 5−10 s, which eliminates adventitious carbon, hydrocarbons and hydroxyl groups as confirmed by X-ray photoelectron spectroscopy (XPS). Metallic clamps integrated with the UPS workfunction sample holder provided electrical contact between the FeF_2 films and the body of the spectrometer, thus eliminating charging. For the UPS measurements with He−Iα excitation, the samples were biased at −9 V dc in order to clearly observe the secondary electron cutoff, and a pure gold specimen was used as a reference to calibrate the workfunction of the spectrometer. The measured Au workfunction was 4.82 eV and the spectrometer workfunction was 8.91 eV. Workfunction was determined according to $\Phi = h\nu - \Delta E$, where ΔE is the energy difference between the secondary electron cutoff of the specimen and the spectrometer workfunction. Electrical properties were measured with an Ecopia HMS5000 Hall mobility system. The optical absorption edge was determined using a Shimadzu UV−vis−NIR spectrophotometer (190−1000 nm). Photoluminescence (PL) and photoluminescence excitation (PLE) characterization were performed at room temperature using a reconfigurable optical bench, which includes two Cornerstone MS257 monochromators, reflective optics, and a photomultiplier tube detector. An ozone-free quartz-tungsten-halogen lamp is the excitation source and lock-in detection is used to minimize background signals.

RESULTS AND DISCUSSION

The bright- and dark-field TEM images a and b in Figure 1 reveal that the deposition conditions used in this study produced polycrystalline films with an overlapping, columnar grain structure. Figure 1c is a high-resolution TEM image of the grain structure and shows the partial grain overlapping. The overlap between grains G1 and G2 creates a Moire pattern that resembles a "crystal lattice" in the region of overlap, and which is identified by the optical Fourier diffraction pattern shown in the inset to Figure 1c. The lattice fringes correspond to the (110) family of planes and the projection of the *c*-axis lattice parameter onto the HRTEM image plane is shown by the yellow vectors. Figure 1d is a representative selected area electron diffraction (SAED) pattern of the grown material. The inset shows the experimental rotationally averaged SAED pattern, together with the theoretical pattern (represented by the red lines) computed with DigitalMicrograph for FeF_2 using the *d*-spacings from the standard JCPDS files. As can be ascertained from examination of the inset, an excellent match is obtained between the experimental and calculated patterns which identifies the structure as polycrystalline FeF_2 having tetragonal $P4_2/mnm$ symmetry and lattice parameters: $a = b =$ 4.6974 and $c = 3.3050$ Å. This is a strong indication that only FeF_2 was grown: no iron oxide phases were detected. Although no iron oxide phases were detected, electron energy loss spectroscopy (EELS) did reveal the presence of atomic oxygen at the FeF_2/Si interface. It can be expected that where atomic oxygen is present it will produce states in the FeF_2 bandgap, but more detailed studies are required to determine the specific correlation. We have performed extensive TEM and EELS chemical analysis of the Si/FeF_2 interface and the FeF_2 film proper, and will report the details of the growth mechanism elsewhere.

Figure 2a is representative of the UPS spectra that are obtained with 40.8 eV He−II excitation from surface-cleaned, ∼400 nm thick, pulsed laser deposited FeF_2 films without bias. Starting with the high spin d^6 ground state, photoionization will

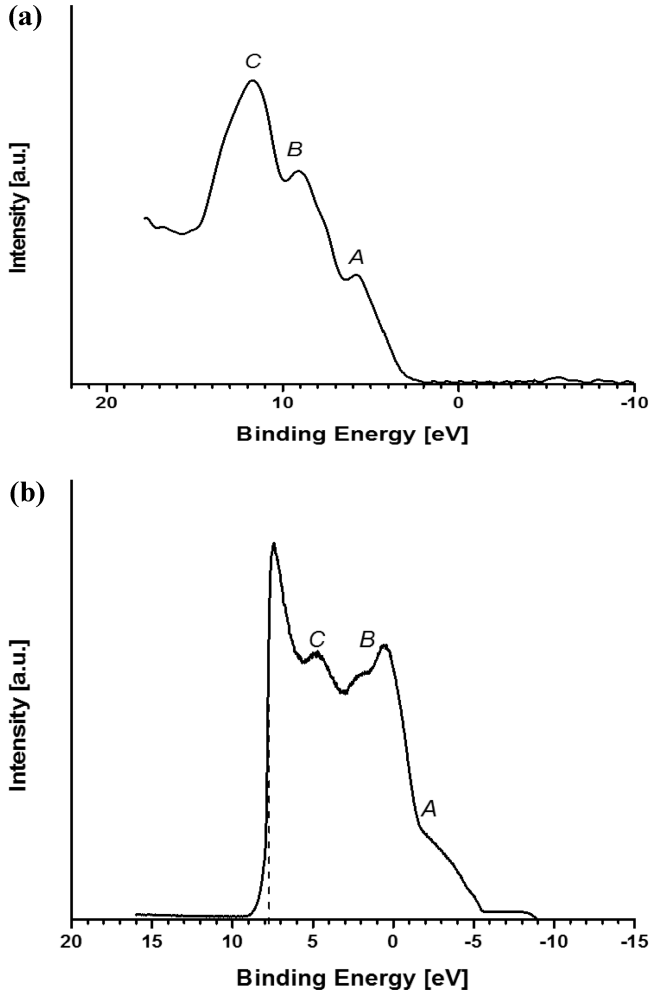

Figure 2. Ultraviolet photoelectron (UPS) spectrum of 400 nm thick PLD FeF_2 film with (a) He−II excitation (40.8 eV) and (b) He−I excitation (21.22 eV). The labels *A* and *B* indicate the Fe d^5 sextet ($^6A_{1g}$) and quartet manifold ($^4T_{1g}$, $^4T_{2g}$, $^4A_{1g}$, $^4E(G)$), respectively. The feature labeled *C* has been ascribed to F^- 2p valence states.

remove an electron from the Fe (Fe^{2+} to Fe^{3+}) and the Tanabe-Sugano[19] d^5 diagram applies. The d^5 diagram indicates that the feature labeled *A* should be assigned to Fe 3d $^6A_{1g}$ sextet states, whereas the feature labeled *B* should be assigned to the 3d quartet manifold ($^4T_{1g}$, $^4T_{2g}$, $^4A_{1g}$, $^4E(G)$). The feature labeled *C* has been ascribed to F 2p valence states.[17] Figure 2b is the UPS spectrum obtained from the same sample spot using 21.22 eV He−Iα radiation. In this case, the sample was biased at −9 V dc in order to observe and measure the secondary electron cutoff, which is necessary to determine the workfunction. Comparison of panels a and b in Figure 2 shows that the same peak positions are observed in the spectra excited with He−II and He−Iα radiation, but that the peak intensity distributions are different. Based on a secondary electron cutoff of 7.8 eV and a spectrometer workfunction of 8.91 eV, the local workfunction of the FeF_2 film was determined to be 4.51 eV. The measurement error is ±0.01 eV. For perspective, this compares to 4.75 and 5.35 eV for wide bandgap SiC and AlN, respectively.[20] It must be stressed that because of the nature of the PLD process, the measured workfunction will be a local value, and variations can be expected from one area to the next of the FeF_2 surface being interrogated. Specifically, because the energy distribution of the PLD flux is nonuniform, the energy

dx.doi.org/10.1021/am3017569 | ACS Appl. Mater. Interfaces 2013, 5, 2387−2391

transferred to the growing film from the plume by momentum transfer (atomic peening) will be different for different areas of the growing sample. As a result, the types and concentrations of defects, and as a consequence the Fermi level position, can be expected to vary across the deposited area. Workfunctions as high as 4.66 eV have been measured for other areas of the same sample. A workfunction of 4.51 eV suggested that the FeF_2 was n-type, and Hall measurements were performed on 400 nm thick films on glass substrates to determine the specific electrical characteristics. On the basis of the general condition that Ohmic contacts require the workfunction of the metal to be smaller than that of the n-type semiconductor, indium (Φ_{In} = 4.1 eV) was evaporated through a shadow mask that produced Ohmic contacts to the FeF_2 in the Van der Pauw contact arrangement. The room temperature Hall measurements further confirmed that as-deposited FeF_2 is n-type: the Hall coefficients were negative, electron mobility was 0.33 $cm^2/(V\ s)$ and resistivity was 0.255 Ω cm. The photoluminescence spectrum of 400 nm thick films on Si substrates is presented in Figure 3. The emission is dominated by two strong, relatively

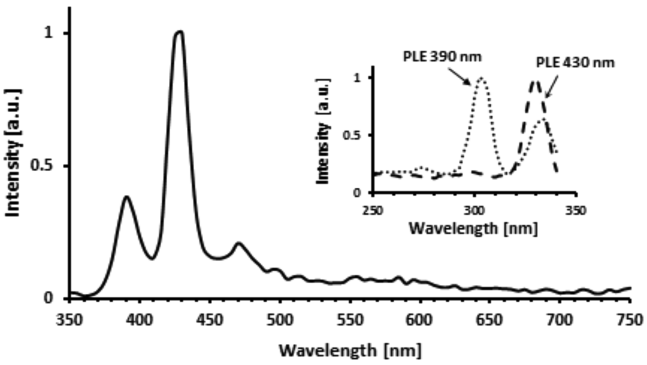

Figure 3. Photoluminescence (PL) spectrum of the FeF_2 films. The inset shows the photoluminescence excitation (PLE) spectra of the 390 and 430 nm emission peaks.

narrow bands peaking at 390 nm/3.18 eV and 430 nm/2.92 eV, respectively. The fwhm of the 390 nm peak is 23 nm whereas the fwhm of the 430 nm band is 18 nm. A weaker, less defined band is observed around 475 nm/2.61 eV. As the inset to Figure 3 shows, the 390 nm emission is optimally excited by 300 nm/4.13 eV light, whereas the 430 nm emission is best excited by 330 nm/3.76 eV. The excitation maximum of the 475 nm band emission is at 365 nm/3.4 eV (not included for brevity). Figure 4 is a Tauc $(h\nu\alpha)^2$ vs $h\nu$ plot that was obtained

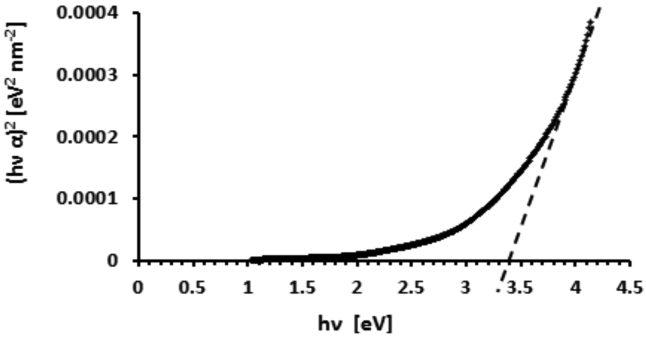

Figure 4. Tauc plot from absorption measurements showing a bandgap of 3.4 eV.

from optical absorption measurements of 120 nm thick films on glass. An optical absorption edge of 3.4 eV is evident. On the basis of the UPS, PL, PLE, and optical absorption data, Figure 5 is the schematic diagram of the energy band structure of FeF_2.

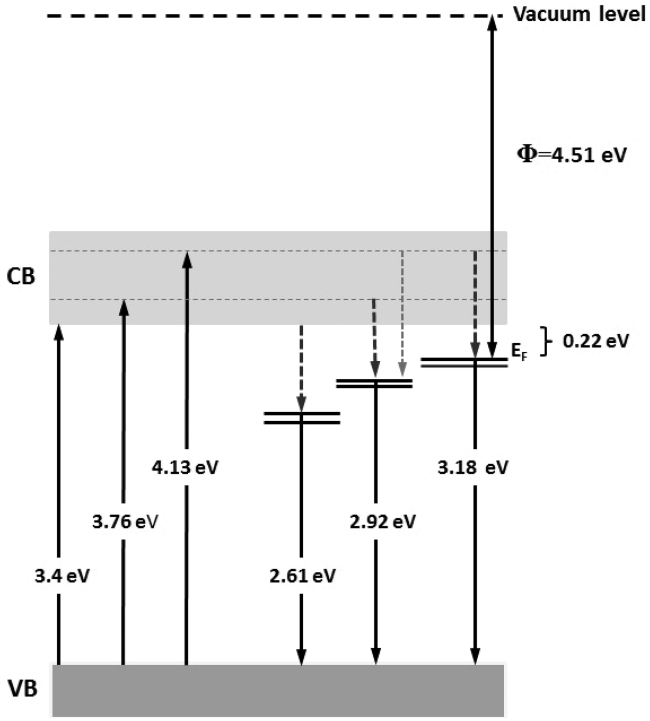

Figure 5. Schematic band diagram constructed from the UPS, PL, PLE and absorption data. The solid upward arrows show excitation, solid downward arrows are radiative relaxations, and the dashed downward arrows indicate nonradiative relations. CB connotes conduction band and VB connotes valence band.

A comprehensive understanding of the band structure of FeF_2 provides insight to mechanism of electron transport in the material for battery applications, and guides the selection of current collectors that facilitate electron flow in and out of the FeF_2 thin film electrode (i.e., provide Ohmic contacts). It should be noted that the band diagram obtained for the FeF_2 thin films also applies to FeF_2 powder electrodes because the particle sizes typically range from several tens to several hundreds of nanometers, and therefore quantum confinement effects on the band structure are not germane. As mentioned earlier, FeF_2 powders are often used with amorphous carbon or graphitic binders to facilitate electronic conduction. However, we note that the FeF_2/graphite interface is an electrical heterojunction, and, that the reported workfunction of graphite ranges between 4.4 eV and 5.2[21−24] depending on structural variations. This means that for $\Phi_{graphite} < \Phi_{FeF2}$, the desirable case of an Ohmic contact that facilitates electron flow in both directions (during charge and discharge) results, whereas for $\Phi_{graphite} > \Phi_{FeF2}$, a Schottky contact that is more conducive to current flow in one direction only would be obtained. The simplified equilibrium band alignment for both cases is explicitly shown in Figure 6 for ideal FeF_2/graphite interfaces, i.e., without interface states. Thus, although this study focused on FeF_2 thin films, the results are applicable to and provide insight to the electronic structure of the traditional FeF_2 powder/graphite composite electrode. The above considerations clearly indicate that more careful attention to electronic

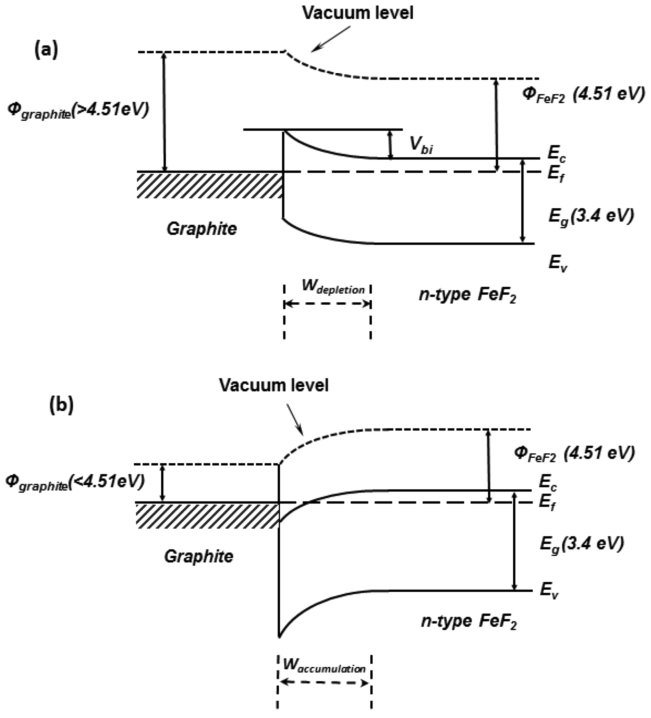

Figure 6. Schematic equilibrium band diagrams for FeF_2/graphite heterojunctions showing the influence of the graphite workfunction. (a) $\Phi_{graphite}>\Phi_{FeF2}$ and a Schottky contact is obtained (b) $\Phi_{graphite}<\Phi_{FeF2}$ and an Ohmic contact is obtained which is desirable for electron flow in both directions. E_c, E_v, E_f, and E_g are the conduction band, valence band, Fermi level, and bandgap, respectively. $W_{accumulation}$ is the accumulation region that forms in the case of the Ohmic contact and $W_{depletion}$ is the depletion region that forms in the case of the Schottky contact.

transport factors even in the case of traditional powders could result in higher battery currents, and highlight the need for more synergy between electrochemical studies and a deeper understanding of electron transport in battery materials.

CONCLUSIONS

To summarize, the pulsed laser deposition conditions used in this work produced near stoichiometric, single phase FeF_2. Our measurements indicate that FeF_2 is a direct bandgap, n-type semiconductor whose band structure is characterized by a 3.4 eV bandgap, a workfunction of ~4.51−4.66 eV, and an effective Fermi level that resides approximately 0.22 eV below the conduction band edge. Stable, low workfunction metals such as Al (Φ = 4.19 eV), Ga (Φ = 4.25 eV), or In (Φ = 4.1 eV)[25] will provide Ohmic contacts to FeF_2 films, and are therefore suitable for use as current collectors. Two relatively shallow, narrow quasi bands presumably due to structural defects reside at 0.22 and 0.48 eV below the conduction band edge, and are responsible for the 390 and 430 nm photoluminescence, respectively. We hypothesize that these two bands, in particular the one at 0.22 eV, serve as shallow donor levels and are responsible for the measured n-type conductivity. The broader, less-well-defined photoluminescence feature at 475 nm apparently originates from a deeper lying, broader defect band. More studies are underway to understand the structural origins of these gap states, to quantitatively determine their concentrations, and to identify the specific electron scattering mechanisms.

AUTHOR INFORMATION

Corresponding Author

*E-mail: Nigel.Shepherd@unt.edu.

Notes

The authors declare no competing financial interest.

ACKNOWLEDGMENTS

This work was supported by the U.S. Department of Energy, Office of Science, and Brookhaven National Laboratory through the Visiting Faculty Program.

REFERENCES

(1) Cabana, J.; Monconduit, L.; Larcher, D.; Palacín, M. R. *Adv. Mater.* **2010**, *22*, E170−E192.
(2) Zu, C.; Li, H. *Energy Environ. Sci.* **2011**, *4*, 2614−2624.
(3) Poizot, P.; Laruelle, S.; Grugeon, S.; Dupont, L.; Tarascon, J. M. *Nature* **2000**, *407*, 496−499.
(4) Poizot, P.; Laruelle, S.; Grugeon, S.; Tarascon, J. M. *J. Electrochem. Soc.* **2002**, *149*, A1212−A1217.
(5) Pereira, N.; Klein, L. C.; Amatucci, G. G. *J. Electrochem. Soc.* **2002**, *149*, A262−A271.
(6) Silva, D. C. C.; Crosnier, O.; Ouvrard, G.; Greedan, J.; Safa-Sefat, A.; Nazar, L. F. *Electrochem. Solid-State Lett.* **2003**, *6*, A162−A165.
(7) Wang, Y.; Fu, Z.; Yue, X.; Qin, Q. *J. Electrochem. Soc.* **2004**, *151*, E162−E167.
(8) Oumellal, Y.; Rougier, A.; Nazri, G. A.; Tarascon, J. M.; Aymard, L. *Nat. Mater.* **2008**, *7*, 916−921.
(9) Tarascon, J. M. *Philos. Trans. R. Soc. London, Ser. A* **2010**, *368*, 3227−3241.
(10) Rockett, A.; Chung, Y. W.; Blaschek, H.; Butterfield, S.; Chance, R. R.; Ferekides, C.; Robinson, M.; Snyder, S. W.; Thackeray, M. *Curr. Opin. Solid-State Mater. Sci.* **2011**, *15*, 8−15.
(11) Badway, F.; Pereira, N.; Cosandey, F.; Amatucci, G. G. *J. Electrochem. Soc.* **2003**, *150*, A1209−A1218.
(12) Makimura, Y.; Rougier, A.; Tarascon, J. M. *Appl. Surf. Sci.* **2006**, *252*, 4587−4592.
(13) Wang, F.; Robert, R.; Chernova, N. A.; Pereira, N.; Omenya, F.; Badway, F.; Hua, X.; Ruotolo, M.; Zhang, R.; Wu, L.; Volkov, V.; Su, D.; Key, B.; Whittingham, M. S.; Grey, C. P.; Amatucci, G. G.; Zhu, Y.; Graetz, J. *J. Am. Chem. Soc.* **2011**, *133*, 18828−18836.
(14) Bates, J. B.; Dudney, N. J.; Neudecker, B.; Ueda, A.; Evans, C. D. *Solid State Ionics* **2000**, *135*, 33−45.
(15) Pištora, J.; Lesňák, M.; Lišková, E.; Višňovský, Š.; Harward, I.; Maslankiewicz, P.; Balin, K.; Celinski, Z.; Mistrík, J.; Yamaguchi, T.; Lopusnik, R.; Vlček, J. *J. Phys. D: Appl. Phys.* **2010**, *43*, 1−6.
(16) Riley, J. D.; Jenkin, J. G.; Liesegang, J.; Leckey, R. C. G. *Phys. Rev. B.* **1976**, *13*, 2620−2624.
(17) Wertheim, G. K.; Guggenheim, H. J.; Hufner, S. *Phys. Rev. Lett.* **1973**, *30*, 1050−1053.
(18) Rangan, S.; Thorpe, R.; Bartynski, R. A.; Sina, M.; Cosandey, F.; Celik, O.; Mastrogiovanni, D. D. T. *J. Phys. Chem.* **2012**, *116*, 10498−10503.
(19) Tanabe, Y.; Sugano, S. *J. Phys. Soc. Jpn.* **1954**, *9*, 766−779.
(20) Pelletier, J.; Gervais, D.; Pomot, C. *J. Appl. Phys.* **1984**, *55*, 994−1002.
(21) Taft, E.; Apker, L. *Phys. Rev.* **1955**, *99*, 1831−1832.
(22) Suzuki, S.; Bower, C.; Kiyokura, T.; Nath, K. G.; Watanabe, Y.; Zhou, O. *J. Electron Spectrosc. Relat. Phenom.* **2001**, *114−116*, 225−228.
(23) Sque, S. J.; Ewels, C. P.; Jones, R.; Briddon, P. R. *Phys. Status Solidi A* **2007**, *204*, 2898−2902.
(24) Ooi, N.; Rairkar, A.; Adams, J. B. *Carbon* **2006**, *44*, 231−242.
(25) Trasatti, S. *J. Chem. Soc., Faraday Trans. 1* **1972**, *68*, 229−236.